Photocytotoxicity and Photoinduced Phosphine Ligand Exchange in a Ru(II) Polypyridyl Complex

Sean J. Steinke,[‡] Sayak Gupta,[†] Eric J. Piechota,[‡] Curtis E. Moore,[‡] Jeremy J. Kodanko,[†]* and Claudia Turro[‡]*

[‡]Department of Chemistry and Biochemistry, The Ohio State University, Columbus, OH 43210 [†]Department of Chemistry, Wayne State University, Detroit, MI 48208

Abstract. Two new tris-heteroleptic Ru(II) complexes with triphenylphosphine (PPh₃) coordination, *cis*-[Ru(phen)₂(PPh₃)(CH₃CN)]²⁺ (1a, phen = 1,10-phenanthroline, PPh₃ = triphenylphosphine) and *cis*-[Ru(biq)(phen)(PPh₃)(CH₃CN)]²⁺ (2a, biq = 2,2'-biquinoline), were synthesized and characterized for photochemotherapeutic applications. Upon absorption of visible light, 1a exchanges a CH₃CN ligand for a solvent water molecule. Surprisingly, the steady-state irradiation of 2a followed by electronic absorption and NMR spectroscopies reveals the photosubstitution of the PPh₃ ligand. Phosphine photoinduced ligand exchange with visible light from a Ru(II) polypyridyl complex has not previously been reported, and calculations reveal that it results from a *trans*-type influence in the excited state. Complexes 1a and 2a are not toxic against triple negative breast cancer cell line MDA-MB-231 in the dark, but upon irradiation with blue light, the activity of both complexes increases by factors of >4.2 and 5.8, respectively. Experiments with PPh₃ alone show that the phototoxicity observed for 2a does not arise from the released phosphine ligand, indicating the role of the photochemically generated ruthenium aqua complex on the biological activity. These complexes represent a new design motif for the selective release of PPh₃ and CH₃CN for use in photochemotherapy.

^{*}Corresponding Authors: C. Turro: turro.1@osu.edu; J. J. Kodanko: jkodanko@wayne.edu

Introduction

Ruthenium(II) polypyridyl complexes exhibit useful excited state properties that have been explored in photochemotherapy (PCT), photodynamic therapy (PDT), and solar energy conversion, among other applications.^{1–8} The spatiotemporal control possible with these complexes shows promise in alternative cancer therapies, circumventing systemic toxicity present in traditional cancer therapies, such as approved platinum drugs.⁹ Typically, PCT and PDT agents are activated by the absorption of visible light in the irradiated area, leading to the population of excited states that can produce cytotoxic ${}^{1}O_{2}$ for PDT or induce the release of a therapeutic agent in PCT. Unlike complexes used in photochemotherapy, PDT agents rely on the presence of oxygen, which can represent a drawback in the hypoxic environments found in solid tumors, ${}^{10-12}$ making PCT agents an important area of research to advance photoinduced treatments.¹³⁻¹⁵

Coordination to the Ru(II) center through a Lewis basic site, such as a nitrile or pyridine functional group, have been explored as PCT agents and for dual PCT/PDT activity, since many drugs that can be photoreleased possess one of these groups able to coordinate to a transition metal center. A frequent challenge, however, is the ability of other strong field ligands, such as phosphines, to undergo photoinduced dissociation. Importantly, molecules with a triphenylphosphinium group and cationic compounds with a triphenyl phosphine (PPh₃) ligand have been shown to enhance cellular uptake, leading to an interest in the investigation of divalent ruthenium triphenyl phosphine complexes for PCT.

Phosphine ligands, such as PMe₃ (Me = methyl) and PPh₃, have been shown to act as ancillary ligands that increase or promote the photosubstitution of other monodentate ligands in the Ru(II) coordination sphere.^{23–25} In particular, PR₃ (R = Me, Ph) ligands are generally stronger field ligands relative to N–coordinated pyridine and acetonitrile. Strong π -backbonding to phosphine ligands has also been used to modify the electronic structure on the ruthenium center to reduce the overpotential of CO₂ reduction catalysts and to tune the absorption and emission properties.^{26–29} Whereas CH₃CN and pyridine have been previously shown to undergo photoinduced ligand exchange in Ru(II) complexes, phosphine ligands are largely inert to

photosubstitution.^{4,24,29–34} The design of complexes that can selectively photodissociate phosphines can enable the use of drugs with phosphine motifs in PCT,^{35–37} as well as the synthesis of supported catalysts patterned with selective irradiation.^{38–40}

In the present work, two new heteroleptic Ru(II) complexes containing one PPh₃ and one CH₃CN ligand, cis-[Ru(phen)₂(PPh₃)(CH₃CN)]²⁺ (**1a**, phen = 1,10-phenanthroline) and cis- $[Ru(biq)(phen)(PPh_3)(CH_3CN)]^{2+}$ (2a, biq = 2,2'-biquinoline), were synthesized and characterized, and their structures are shown in Figure 1. The electronic absorption, electrochemistry, and photochemistry of 1a and 2a were investigated and compared to those of their bis-acetonitrile analogs, cis-[Ru(phen)₂(CH₃CN)₂]²⁺ (**1b**) and cis-[Ru(biq)(phen)(CH₃CN)₂]²⁺ (**2b**). Based on the steric distortion introduced by the bulky PPh₃ ligand, complexes 1a and 2a were expected to exhibit more facile CH₃CN dissociation. While **1a** exhibits photoinduced CH₃CN exchange upon visible light excitation, 2a represents the first example of photoinduced exchange of a PPh₃ ligand from a Ru(II) polypyridyl complex, a surprising departure from the commonly observed substitutional inertness of PPh₃ ligands. Single-crystal X-ray structures of 1a, 2a, and 2b, the photoproduct of 2a following photolysis in CH₃CN and pyridine, were collected and calculations were performed on 1a and 2a to gain better understanding of the origin of the unusual photoreactivity. In addition, complexes 1a and 2a were evaluated for their toxicity against the triple-negative breast cancer MDA-MB-231 cell line in the dark and upon irradiation. The present findings show enhanced activity following photoinduced ligand dissociation for both complexes and that PPh₃ release from 2a results in a modest increase in toxicity as compared to CH₃CN photodissociation in 1a. Importantly, both 1a and 2a exhibit significantly greater photoactivity than related complexes without PPh₃ in their coordination sphere. The present work is consistent with greater cellular uptake by the PPh₃-containing complexes, laying the groundwork for the design of new photoactive complexes with enhanced activity.

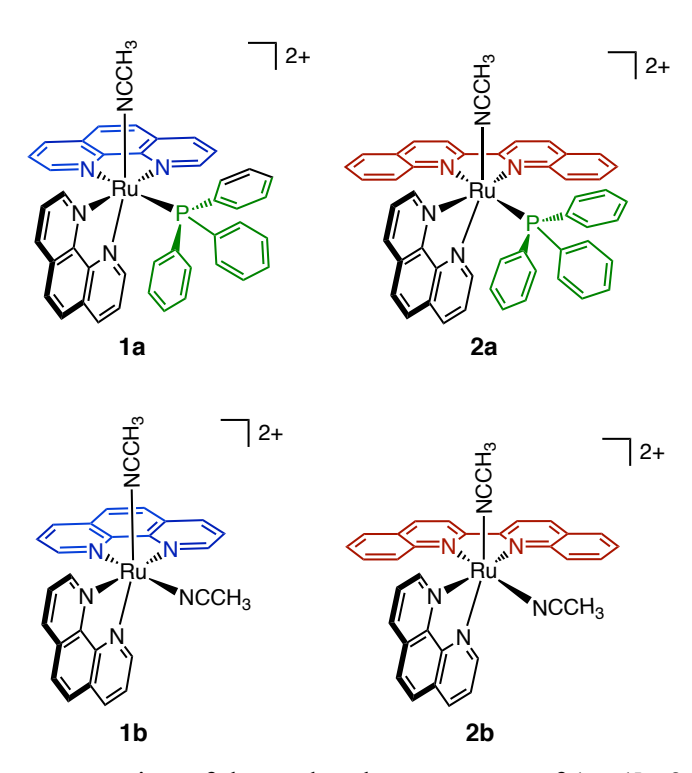


Figure 1. Schematic representation of the molecular structures of 1a, 1b, 2a, and 2b.

Experimental

Materials. All materials were used as received without further purification, including1,10-phenanthroline, 2,2'-biquinoline, CD₃CN, CD₃OD, (CD₃)₂CO, lithium chloride, pyridine, silver tetrafluoroborate, tetrabutylammonium hexafluorophosphate, and triphenylphosphine which were purchased from Sigma-Aldrich. Ethanol (200 proof) was obtained from Decon Laboratories, acetone, acetonitrile, dichloromethane, diethyl ether, *N*,*N*-Dimethylformamide, 85% H₃PO₄, and toluene were acquired from Fischer Scientific, and ammonium hexafluorophosphate was purchased from Oakwood Chemical. Complexes **1b** and **2b**,⁴¹ [Ru(phen)₂Cl₂],⁴² [Ru(pcymene)Cl₂]₂,⁴³ and triphenylphosphine oxide⁴⁴ were prepared according to literature procedures.

[Ru(phen)₂(PPh₃)(Cl)](PF₆). [Ru(phen)₂Cl₂] (0.16 g, 0.30 mmol), triphenylphosphine (0.14 g, 0.53 mmol), and excess LiCl were added to 10 mL ethanol/water (1:1, v:v) mixture sparged 15 min with N₂. The reaction mixture was refluxed for 4 h under a nitrogen atmosphere, allowed to cool, concentrated by rotary evaporation, and then precipitated by adding it dropwise to a

concentrated NH₄PF₆ solution. The product was purified by column chromatography, using a deactivated neutral alumina stationary phase and a 1:2 toluene:acetone mobile phase. The solvent was removed from the fraction containing the product via rotary evaporation, producing a dark orange solid (0.078 g, 29% yield). ¹H NMR (400 MHz, (CD₃)₂CO, Figure S1): δ 9.72 (d, 1H, J = 5.4 Hz), 8.77 (m, 2H), 8.68 (d, 1H, J = 8.2 Hz), 8.55 (dd, 1H, J = 5.7, 3.9 Hz), 8.37 (s, 2H), 8.36 (d, 1H, J = 1.3 Hz), 8.30 (d, 1H, J = 8.8), 8.23 (dd, 1H, J = 20.3, 9.0 Hz), 8.13 (d, 1H, J = 8.8 Hz), 7.90 (dd, 1H, J = 8.2, 5.3 Hz), 7.86 (dd, 1H, J = 8.2, 5.3 Hz), 7.77 (dd, 2H, J = 8.3, 5.3 Hz), 7.65 (d, 1H, 5.3 Hz), 7.53 (m, 2H), 7.37 (t, 5H, J = 8.7 Hz), 7.27 (t, 2H, J = 7.6 Hz), 7.11 (m, 6H). ³¹P{H} NMR (400 MHz, (CD₃)₂CO, Figure S2): δ 45.1 (s, 1P).

[Ru(phen)₂(**PPh**₃)(**CH**₃**CN**)](**PF**₆)₂ (**1a**). [Ru(phen)</code>₂(**PPh**₃)Cl](**PF**₆) (0.058 g, 0.064 mmol) was dissolved in 10 mL of acetonitrile/H₂O (1:1, v:v) mixture and, under an atmosphere of nitrogen, was refluxed overnight. After cooling to room temperature, the reaction solution was added dropwise to a concentrated aqueous NH₄PF₆ solution. The precipitate that formed was collected by filtering over Celite and purified on a neutral alumina column eluted with a 1:2 toluene:acetone mobile phase. The purified solution was collected and the solvent was removed *via* rotary evaporation, affording the desired product as a yellow-orange solid (0.031 g, 53% yield). ¹H NMR (400 MHz, CD₃CN, Figure S3): δ 9.41 (d, 1H, J = 5.3 Hz), 9.09 (d, 1H, J = 5.2 Hz), 8.82 (dd, 1H, J = 8.4, 1.2 Hz), 8.59 (dd, 1H, J = 8.3, 1.2 Hz), 8.55 (dd, 1H, J = 8.2, 1.3 Hz), 8.37 (dd, 1H, J = 8.3, 1.2 Hz), 8.24 (dd, 2H, J = 28, 8.8 Hz), 8.13 (dd, 2H, J = 18, 8.8 Hz), 7.90 (dd, 1H, J = 3.0, 5.3 Hz), 7.75 (dd, 1H, J = 3.0, 5.3 Hz), 7.49 (m, 1H), 7.43 (m, 1H), 7.37 (m, 4H), 7.19 (m, 7H), 7.03 (td, 6H, J = 9.4, 1.1 Hz), 2.17 (s, 3H). ³¹P{H} NMR (400 MHz, CD₃CN, Figure S4): δ 45.3 (s, 1P). ESI-MS(+): [M – PF₆]⁺ m/z = 910.193 (calc. m/z = 910.123).

[Ru(p-cymene)(phen)Cl]. [Ru(p-cymene)Cl₂]₂ (0.30 g, 0.50 mmol) and 1,10-phenanthroline (0.19 g, 1.1 mmol) were dissolved in 4 mL acetonitrile and refluxed under a nitrogen atmosphere for 2 h, during which time a change from a red to orange solution was observed. A yellow-orange solid was collected by filtering over Celite (0.37 g, 82% yield). ¹H NMR (400 MHz, CD₃OD,

Figure S5): δ 9.84 (d, 2H, J = 5.5 Hz), 8.84 (d, 2H, J = 8.3 Hz), 8.21 (s, 2H), 8.11 (dd, 2H, J = 8.3, 5.3 Hz), 6.23 (d, 2H, J = 6.5 Hz), 6.00 (d, 2H, J = 6.2 Hz), 2.66 (q, 1H, J = 7.0 Hz), 2.27 (s, 3H), 0.99 (d, 6H, J = 6.9 Hz).

[Ru(biq)(phen)Cl₂]. [Ru(p-cymene)(phen)Cl] (0.33 g, 0.68 mmol), 2,2'-biquinoline (0.18 g, 0.69 mmol), and excess LiCl were dissolved in 2 mL *N*,*N*-dimethylformamide and refluxed under a nitrogen atmosphere for 90 min. After refluxing was complete, the reaction mixture was allowed to cool to room temperature and then added dropwise to 30 mL aqueous LiCl solution, producing a dark green solution. A dark green solid was collected *via* vacuum filtration and was rinsed three times each with 20 mL H₂O and 20 mL diethyl ether. The solid was dissolved using 1 L of a CH₂Cl₂/methanol (1:1, v:v) solvent mixture, which was then removed by rotary evaporation to afford the desired product as a dark green solid (0.18 g, 44% yield).

[Ru(biq)(phen)(PPh₃)Cl](PF₆). [Ru(biq)(phen)Cl₂] (0.048 g, 0.080 mmol), triphenylphosphine (0.039 g, 0.15 mmol), and excess LiCl were added to a 10 mL ethanol/water (1:1, v:v) mixture sparged 15 min with N₂. The reaction mixture was refluxed 4 h under a nitrogen atmosphere, allowed to cool, concentrated by rotary evaporation, and then added dropwise to a concentrated NH₄PF₆ solution to produce a purple precipitate. The product was purified by column chromatography, using a neutral alumina stationary phase and an acetone mobile phase. The solvent was removed from the fraction containing the product *via* rotary evaporation producing a red-purple solid (0.052 g, 66% yield). ¹H NMR (400 MHz, (CD₃)₂CO, Figure S6): δ 10.21 (s, 1H), 8.90 (m, 4H), 8.61 (d, 2H, J = 7.8 Hz), 8.53 (d, 1H, J = 8.1 Hz), 8.30 (t, 2H, J = 7.3 Hz), 8.12 (d, 1H, J = 8.2 Hz), 8.06 (dd, 1H, J = 8.1, 5.5 Hz), 7.85 (dd, 3H, J = 32.8, 9.0 Hz), 7.63 (m, 3H), 7.52 (t, 1H, J = 7.6 Hz), 7.28 (t, 2H, 7.5 Hz), 7.17 (s, 3H), 6.95 (m, 12H). ³¹P{H} NMR (400 MHz, (CD₃)₂CO, Figure S7): δ 42.5 (s, 1P).

[Ru(biq)(phen)(PPh₃)(CH₃CN)](PF₆)₂ (2a). [Ru(biq)(phen)(PPh₃)Cl](PF₆) (0.044 g, 0.038 mmol) and AgBF₄ (0.019 g, 0.099 mmol) were dissolved in 10 mL of a CH₃CN/H₂O (1:1, v:v)

mixture and were refluxed overnight under a N_2 atmosphere. After cooling to room temperature, the reaction mixture was added dropwise to a concentrated NH₄PF₆ solution, precipitate was collected by filtering over Celite, and then purified *via* bulk recrystallization using vapor diffusion of ether into a concentrated solution of **2a** in acetonitrile, which afforded a red-orange solid (0.013 g, 35% yield). ¹H NMR (400 MHz, CD₃CN, Figure S8): δ 10.1 (d, 1H, J = 5.3 Hz), 8.96 (d, 2H, J = 8.7 Hz), 8.69 (d, 2H, J = 8.8 Hz), 8.30 (m, 5H), 8.19 (m, 5H), 8.07 (dd, 2H, J = 5.4, 2.8 Hz), 7.64 (m, 4H), 7.54 (m, 5H), 7.28 (td, 3H, J = 7.4, 1.1 Hz), 7.21 (td, 3H, J = 7.8, 1.5 Hz), 7.16 (td, 3H, J = 7.9, 1.4 Hz), 2.34 (s, 3H). ³¹P{H} NMR (400 MHz, CD₃CN, Figure S9): δ 42.3 (s, 1P). ESI-MS(+): [M – PF₆]⁺ m/z = 986.252 (calc. m/z = 986.155).

Instrumentation and Methods. Electronic absorption spectra were collected using a Hewlett-Packard 8454 diode array spectrophotometer in 1 cm x 1 cm quartz cuvettes. The irradiation source for photolysis experiments was a 150 W Xe arc lamp (UHSIO) in a MilliArc lamp housing unit equipped with an LPS-220 power supply and an LPS-221 igniter (PTI). Irradiation wavelengths for quantum yield determination were selected by using bandpass and long-pass filters (CVI Melles Griot). Samples for photolysis were prepared under red light, sealed in an NMR tube (NMR) or cuvette (UV-Vis), and purged with N₂ for 15 min prior to irradiation.

The ¹H and ³¹P{H} NMR spectra were obtained using a Bruker 400 MHz DPX instrument in CD₃CN, (CD₃)₂CO, or CD₃OD. ¹H chemical shifts were referenced to the residual protonated solvent peak and ³¹P{H} shifts were referenced to an external 85% H₃PO₄ standard (0 ppm). ¹H and ³¹P{H} NMR photolysis experiments were performed in CD₃CN. Electrospray ionization mass spectrometry (ESI-MS) was performed using a Bruker microTOF instrument. For ESI-MS experiments, samples were dissolved in CH₃CN and referenced to a sodium trifluoroacetate standard.

Electrochemistry experiments were performed on a BASi model CV-50W voltammetric analyzer (Bioanalytical Systems, Inc.) with a three-electrode cell utilizing a glassy carbon working

electrode, a Pt wire auxiliary electrode, and a saturated Ag/AgCl (3 M NaCl) reference electrode. Samples were dissolved in acetonitrile containing 0.1 M tetrabutylammonium hexafluorophosphate (TBAPF₆) as an electrolyte, data was collected at a scan rate of 200 mV/s, and ferrocene was added at the end of each experiment as an internal reference (+0.43V *vs* Ag/AgCl in acetonitrile).⁴⁵

Crystals suitable for X-ray diffraction were obtained through vapor diffusion of diethyl ether into concentrated acetonitrile or pyridine solutions of the desired complex. Single crystal X-ray diffraction for 2a was performed using a dark red rectangular plate crystal in a nitrogen gas stream at 150 K. The diffraction pattern was collected using a Nonius Kappa APEXII CCD diffractometer and Mo K_{α} radiation ($\lambda = 0.7107$ Å). Data were integrated using the Bruker SAINT software program and scaled using the SADABS software program. Structures were solved and refined with the Bruker SHELXT Software Package within APEX2 and Olex2. Other single crystal x-ray diffraction measurements were performed on a Bruker Kappa Photon II CPAD diffractometer equipped with Mo K_{α} radiation (1a and 2b, $\lambda = 0.71073$ Å) or Cu 1a0 or Cu 1a0 or Cu 1a1 or Cu 1a2 and 1a3 using a dark red crystal (1a3), orange plate (1a4), or red blade (1a5) in a nitrogen gas stream at 1a6 using a dark red crystal (1a6), orange plate (1a7), or red blade (1a8) in a nitrogen gas stream at 1a8 software program. Solution by direct methods (SHELXT) produced a complete phasing model consistent with the proposed structure.

Spin restricted and unrestricted density functional theory (DFT) calculations were performed using the Gaussian09 program package.⁴⁶ Geometry optimizations and vibrational frequency calculations were performed with the SDD⁴⁷ basis set on Ru and the TZVP⁴⁸ basis set on all other atoms with the PBE exchange-correlation functional.^{49,50} The geometries of **1a**, **2a**, and **2b** were fully optimized starting from X-ray crystal structures and were verified to have positive harmonic frequencies, confirming the calculated structures as electronic energy minima. Molecular orbital calculations utilized the hybrid functional B3LYP,^{51–53} with the SDD basis set on Ru and the TZVP basis set on all other atoms. Spin densities were calculated using Mulliken population analysis (MPA) methods. Molecular orbitals from the Gaussian calculations were

plotted using the Chemcraft program,⁵⁴ and the analysis of the molecular orbitals and Mayer bond order calculations were performed using AOMix-FO within the AOMix program.^{55,56}

The cell viability of all the synthesized complexes were determined by plating MDA-MB-231 cells in a 96 well plate at a density of 7000 cells per well in Dulbecco's Modified Eagle's Medium (DMEM) supplemented with 10% FBS and 1,000 units/mL penicillin/streptomycin. The plates were incubated overnight in a 37°C humidified incubator ventilated with 5% CO₂. The media was aspirated off and then quadruplicate wells were treated with DMEM supplemented with 10% FBS and 1,000 units/mL penicillin/streptomycin containing different concentrations (30 μM to 500 nM) of the synthesized complexes in 1% DMSO. Plates containing wells with no cells were designated as blank wells whereas wells with cells that were not treated with the compound but only DMEM supplemented with 10% FBS and 1,000 units/mL penicillin/streptomycin containing 1% DMSO (vehicle) were designated as control wells. The plates were then again incubated in a 37°C humidified incubator ventilated with 5% CO₂. After 1 hr of incubation, the cells were either irradiated with blue light ($t_{irr} = 20 \text{ min}$, $\lambda_{irr} = 460-470 \text{ nm}$, 56 J/cm²) or kept in the dark. After 20 minutes, the plates were placed in a 37°C humidified incubator with 5% CO₂ for 72 hrs, after which time, 10 µL of MTT reagent (5 mg/mL in PBS) was added to each well of the 96 well plate and incubated in a 37°C humidified incubator ventilated with 5% CO₂ for 2 hrs. The media was then aspirated off and 100 µL of DMSO was added. The plates were then shaken for 20 min to ensure complete dissolution of the purple formazan crystals. Absorbance of each well was then measured at 570 nm. The mean absorbance values of the blank wells were calculated and subtracted from absorbance values for each well treated with a certain concentration of a compound. The absorbance of the control wells was also taken and subtracted with the average of the blank wells. The mean of these corrected control absorbances were then calculated. Viability of the cells was finally determined by dividing the corrected absorbance of the compound wells by the mean corrected absorbance of the blank wells and expressing the mean of the ratio as a percentage value. The % Viability was plotted against the log of concentration (in Molarity) of the compounds and the antilog of the concentration value at 50% viability was used to determine the EC₅₀ value of each complex against MDA-MB-231 cells.

Results and Discussion

Electronic Absorption and Electrochemistry

The electronic absorption spectra of 1a, 1b, 2a, and 2b are shown in Figure 2 and the corresponding absorption maxima and extinction coefficients are listed in Table 1. The singlet metal-to-ligand charge transfer (${}^{1}MLCT$) absorption maxima of 1a in CH₃CN, attributed to Ru($d\pi$) \rightarrow phen(π^*) transitions, are observed at 372 nm and 411 nm. For 2a the Ru($d\pi$) \rightarrow phen(π^*) and Ru(π p) \rightarrow biq(π^*) ${}^{1}MLCT$ bands are observed at 407 nm and 477 nm, respectively, in CH₃CN. The substitution of one of the phen ligands in 1a for biq in 2a results in a bathochromic shift in the ${}^{1}MLCT$ absorption maximum, as expected from the increased conjugation and subsequently increased π -accepting character of the biq ligand as compared to phen. A similar shift is observed in the ${}^{1}MLCT$ maxima of the bis-acetonitrile analogs, 1b and 2b, at 420 nm and 497 nm, respectively. In addition, the lower energy of the ${}^{1}MLCT$ transitions in 1b and 2b, as compared to the corresponding peaks in 1a and 2a, are consistent with the increased π -accepting character of the phosphine ligand as compared to acetonitrile. ${}^{26,31,57-59}$

The electrochemical reduction potentials for complexes $\bf 1a$ and $\bf 2a$ obtained from cyclic voltammetry (CV) experiments are listed in Table 1 and the corresponding CVs are shown in Figure S10, and are compared to those previously reported for $\bf 1b$ and $\bf 2b$.⁴¹ The first reversible reduction events of $\bf 1a$ and $\bf 1b$ are localized on one of the phen ligands, with $E_{1/2}$ values at -1.29 V and -1.34 V vs Ag/AgCl, respectively, and compare well to those reported for related complexes.^{60,61} In contrast, the first reduction couples of $\bf 2a$ and $\bf 2b$ observed at -0.82 V and -0.86 V vs Ag/AgCl, respectively, are centered on the biquinoline ligand in each complex, consistent with the lower energy lowest unoccupied π^* orbital in biq and similar to those measured in related complexes.^{60,62}

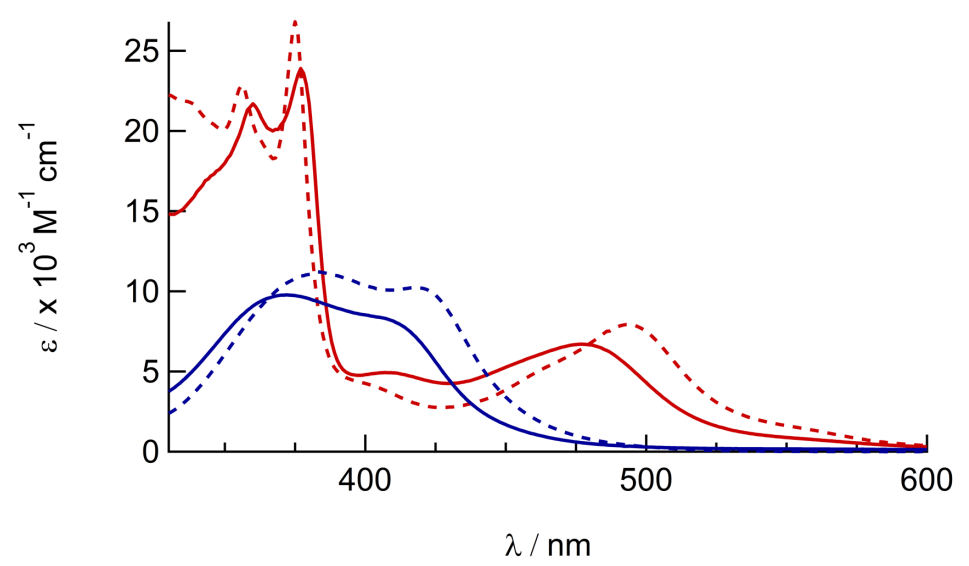


Figure 2. Electronic absorption spectra of 1a (solid blue), 1b (dashed blue), 2a (solid red), and 2b (dashed red) in CH₃CN.

Table 1. Electronic Absorption Maxima (λ_{abs}), Molar Absorption Coefficients (ϵ), and Electrochemical Half-Wave Reduction Potentials ($\epsilon_{1/2}$) in CH₃CN.

Complex	λ_{abs} / nm (ϵ / $x10^3~M^{1}~cm^{1})$	$\mathrm{E}_{\mathrm{1/2}}$ / V^a
1a	372 (9.1), 411 (7.4)	+1.62, -1.29, -1.51
$\mathbf{1b}^{b}$	383 (11.2), 420 (10.2)	+1.50, -1.34, -1.50
2a	360 (18), 377 (20), 407 (4.2), 477 (5.7)	$+1.67, -0.82, -1.36^{c}$
2b ^b	356 (23), 375 (27), 406 (3.9), 497 (7.8)	+1.55, -0.86, -1.40

^a0.1 M TBAPF₆, vs Ag/AgCl in CH₃CN. ^bFrom ref. 41. ^cIrreversible.

The second reduction wave is localized on the phen ligand in 2a and 2b, observed at -1.36 V and -1.40 V vs Ag/AgCl, respectively, and on the remaining phen ligand in 1a and 1b, at -1.51 V and -1.50 V vs Ag/AgCl, respectively. The reversible oxidation events ranging from +1.50 to +1.67 V vs Ag/AgCl are assigned to the Ru^{III/II} redox couple (Figure S10 and Table 1). The ~ 120 mV shift of the Ru^{III/II} couples to more positive potentials in 1a and 2a relative to those in 1b and 2b, respectively, is consistent with the greater π -accepting character of triphenylphosphine,

stabilizing the highest occupied molecular orbital (HOMO). Taken together, the electrochemical data indicate that the synthetic substitution of PPh₃ in $\bf 1a$ and $\bf 2a$ for CH₃CN in $\bf 1b$ and $\bf 2b$ primarily affects the energy of the Ru(d π) t_{2g}-type orbitals.

Photochemistry

In order to explore the light-induced ligand dissociation in complexes 1a and 2a, their photoreactivity was investigated by monitoring changes in the electronic absorption and ¹H and ³¹P{H} NMR spectra as a function of irradiation time. Irradiation of **1a** in water (<5% acetone) with visible light results in a decrease in intensity of the absorption peak at 372 nm and a concomitant increase in the 430 – 550 nm range with a shoulder at 455 nm, along with an isosbestic point at 407 nm (Figure 3a). The presence of the isosbestic point is indicative of the reaction proceeding from the starting material to a single product. The changes to the ¹H NMR spectrum of 1a in CD₃CN were also monitored as a function of irradiation time, resulting in a decrease in the resonance at 2.17 ppm associated with CH₃CN bound to ruthenium and the concomitant appearance of a resonance at 1.96 ppm, corresponding to free CH₃CN (Figure 3b). These data indicate that the irradiation of 1a results in the substitution of the CH₃CN ligand with a solvent molecule, in this case CD₃CN, with the absence of any additional photochemical reactions. The bathochromic shift in Figure 3a is also consistent with this conclusion, as the photolysis of 1a in water results in the formation of cis-[Ru(phen)₂(PPh₃)(H₂O)]²⁺, where the bound CH₃CN is substituted for the weaker-field, π-donating H₂O ligand, thus raising the energy of the Ru(dp) t_{2g}type set and lowering the energy of the ¹MLCT transition. ^{34,63,64}

The irradiation of **2a** in CH₃CN results in a decrease in the absorption at 407 nm and an increase a peak at 497 nm, with two isosbestic points at 396 nm and 478 nm (Figure 4a). As shown in Figure 4b, the spectrum of the photoproduct is nearly identical to that of **2b**, providing evidence that the irradiation of **2a** results in the photoinduced dissociation of the PPh₃ ligand generating *cis*—[Ru(biq)(phen)(CH₃CN)₂]²⁺, compound **2b**. The changes in the ¹H NMR spectra of **2a** in CD₃CN recorded as a function of irradiation time are also consistent with the exchange of the phosphine

ligand following visible light irradiation (Figure 5a). For example, the resonance at 2.34 ppm, associated with the ruthenium-bound CH₃CN ligand, decreases in intensity upon irradiation, with the concomitant growth of a peak at 2.47 ppm, associated with the photoproduct *cis*–[Ru(biq)(phen)(CH₃CN)(CD₃CN)]²⁺, similar to the resonances observed for the coordinated CH₃CN ligands in **2b**.⁴¹

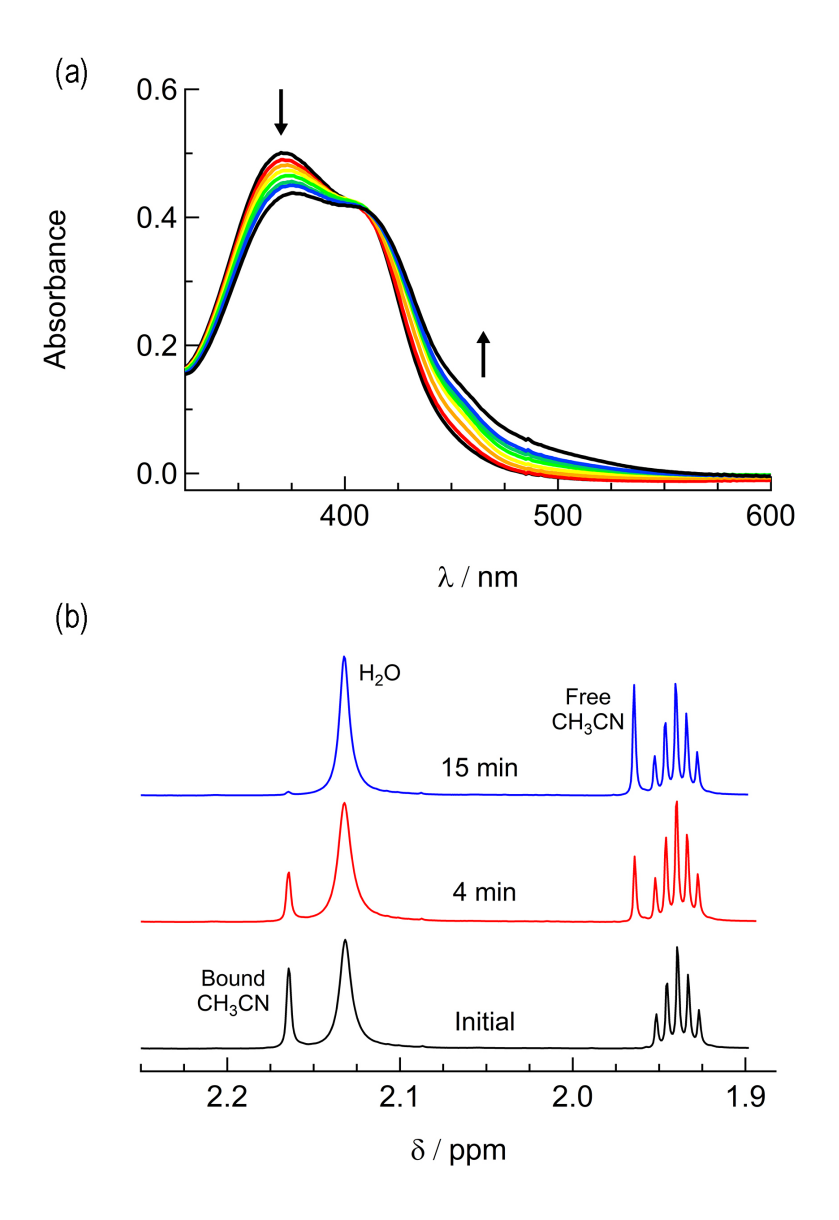


Figure 3. Changes following the irradiation of **1a** ($\lambda_{irr} \ge 395$ nm) to the (a) electronic absorption spectrum in H₂O, $t_{irr} = 0$ -30 min, and (b) ¹H NMR spectrum in CD₃CN, $t_{irr} = 0$, 4, and 14 min.

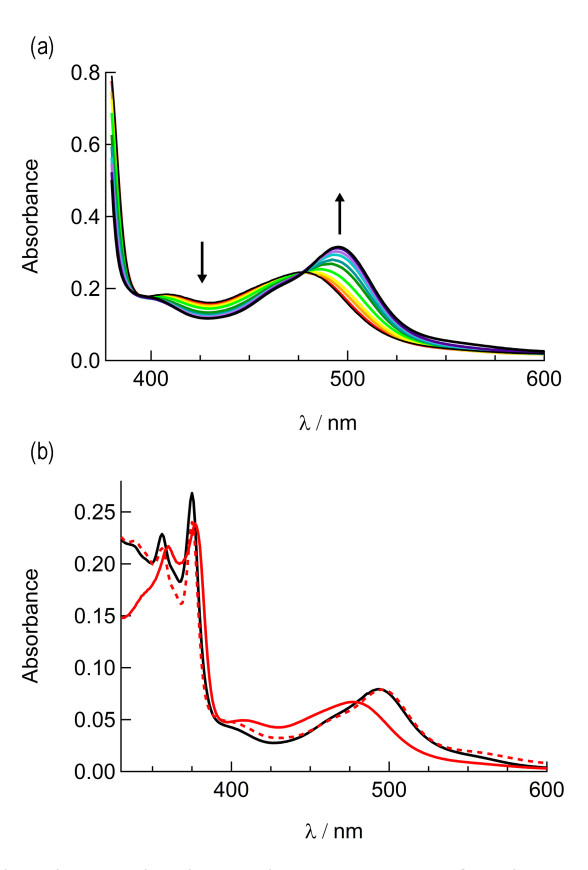


Figure 4. (a) Changes in the electronic absorption spectrum of $\mathbf{2a}$ in CH₃CN following irradiation, $t_{irr} = 0 - 5$ min and (b) electronic absorption spectra of $\mathbf{2a}$ before irradiation (solid red), following 30 min irradiation (dashed red), and $\mathbf{2b}$ (black)

The changes to the ³¹P{H} NMR spectra of **2a** upon irradiation provides additional evidence for PPh₃ exchange, where a decrease in intensity of the ³¹P{H} resonance at 42.3 ppm, associated with coordinated PPh₃ is observed during the photolysis (Figure 5b). Concurrently, a ³¹P{H} resonance corresponding to triphenylphosphine oxide centered at 26.0 ppm appeared as a function of irradiation time (Figures 4d and S11). Importantly, following 15 minutes of irradiation of **2a**, the ³¹P{H} resonance associated with bound PPh₃ completely disappears, while the ¹H peaks of the photoproduct *cis*–[Ru(biq)(phen)(CH₃CN)(CD₃CN)]²⁺ persisted. In addition, the resonance at 1.96 ppm associated with free CH₃CN appears concomitantly with the peak at 2.47 ppm, indicating CH₃CN is also photodissociated albeit not completely on the timescale of the NMR photolysis experiment.

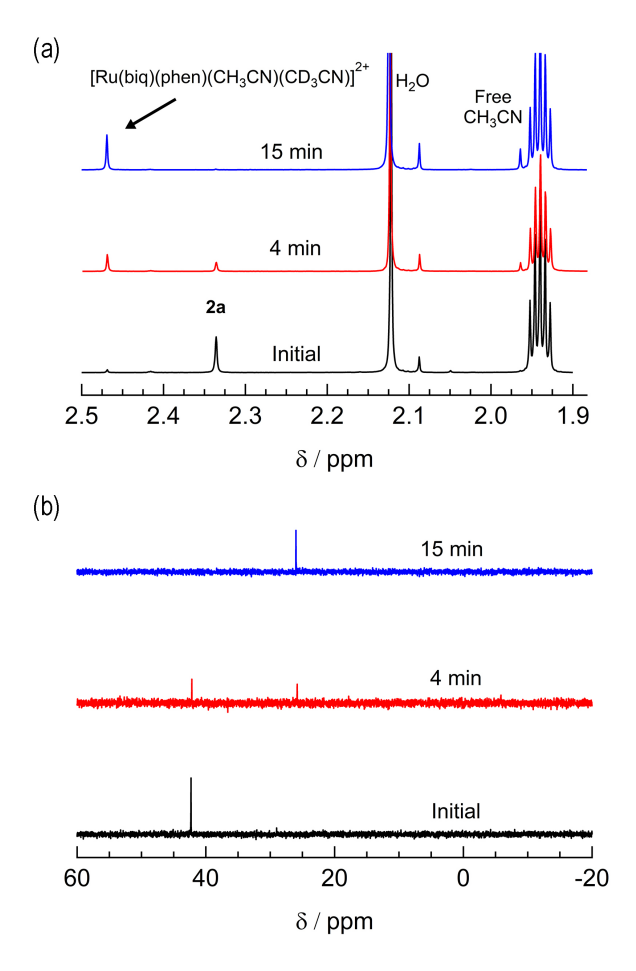


Figure 5. Changes in the (a) 1 H and (b) 31 P{H} NMR spectra of **2a** in CD₃CN at $t_{irr} = 0$, 4, and 15 min ($\lambda_{irr} \ge 395$ nm).

Based on these results, the question remains whether the irradiation of **2a** results in dissociation of both PPh₃ and CH₃CN from the starting material, or if CH₃CN exchanges only from the intermediate photoproduct *cis*–[Ru(biq)(phen)(CH₃CN)(CD₃CN)]²⁺ after the initial dissociation of PPh₃ from the starting complex. In an effort to address this point and trap the product of the first ligand exchange step, photolysis experiments were performed in the coordinating solvent pyridine under identical illumination conditions to those previously discussed in acetonitrile, and the results are shown in Figure 6. Inspection of Figure 6a reveals one set of isosbestic points at early irradiation times, up to ~2.5 min, observed at 316 nm, 448 nm, and 500 nm, and the decrease of the peak associated with **2a** at 490 nm with the appearance of a band at 540 nm. A second set of isosbestic points is evident at later times (Figure 6b), from ~3.5 min to

20 min, at 338 nm, 361 nm, and 550 nm, with a loss of the species with absorption at 540 nm and the formation of the final product with maximum at 590 nm. These results point at the formation of solely one initial intermediate, **I**, with maximum at 540 nm, which then goes on to exchange a second ligand to generate the final product with a peak at 590 nm, assigned to cis–[Ru(biq)(phen)(py)2]²⁺ (3). As expected from the ability of CH₃CN to π -backbond with the Ru(d π) t_{2g}-type orbitals that is not present in pyridine, the ¹MLCT maximum of cis–[Ru(biq)(phen)(py)2]²⁺, 3, is red-shifted compared to that of the product **2b**, cis–[Ru(biq)(phen)(CH₃CN)2]²⁺, in Figure 4a.

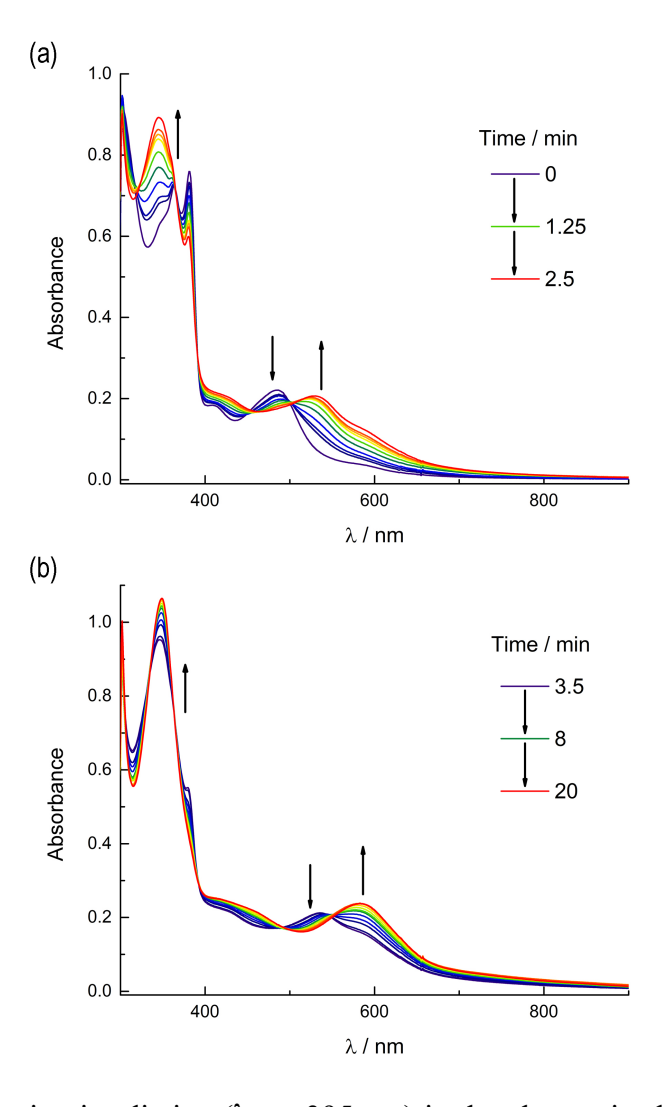


Figure 6. Changes following irradiation ($\lambda_{irr} \ge 395$ nm) in the electronic absorption spectrum of **2a** in pyridine from (a) $t_{irr} = 0 - 2.5$ min and (b) $t_{irr} = 3.5 - 20$ min.

The intermediate **I** was identified as cis–[Ru(biq)(phen)(py)(CH₃CN)]²⁺, generated by absorption of a single photon by **2a** and photosubstitution of the triphenylphosphine ligand for a solvent pyridine molecule. Identification was supported, in conjunction with 31 P{H} NMR spectra (Figure 5b), by obtaining a single-crystal x-ray diffraction structure of the photoproduct generated by irradiating a solution of **2a** in pyridine with \geq 395 nm light for 90 s (Figure S12, Table S1). No further spectral changes took place after the conclusion of irradiation, indicating **I** is stable in the dark. This conclusion further supported by the persistence of the complex in a pyridine solution as the compound recrystallized *via* diethyl ether diffusion.

The presence of the two sets of isosbestic points permits determination of time-dependent concentrations of the three individual species in solution: **2a**, **I**, and **3**, during the photolysis, where **I** represents an intermediate species. The deconvolution of the associated spectra is possible from the known absorption spectra and molar extinction coefficients of **2a** and **3**, and the details of the analysis are presented in the Supplementary Information, Table S2, and Figure S13. The spectra of **2a** and **3**, along with that of the intermediate, **I**, are shown in Figure S13, and the time dependent mole fractions of each species were calculated over the course of the photolysis and are displayed in Figure 7. Figure 7 shows that the loss of **2a** occurs rapidly, whereby at 70 s, 50% of the starting material remains and no amount is appreciable beyond 300 s. The formation of the intermediate **I** begins as early as 50 s of irradiation and reaches 99% conversion to the final product, **3**, at ~900 s. A maximum fraction of ~55% of the intermediate **I** is apparent at ~150 s (Figure 7). From the known proportions of the three species the extinction coefficient for the intermediate was estimated and compared to initial and final product values in Figure S13.

The PPh₃ ligand photodissociation from 2a apparent from the sequential formation of photoproducts in Figures 6 and 7, as well as in the crystal structure of I, shows that irradiation of 2a does not result in the photodissociation of the CH₃CN ligand, such that there there is no evidence of the formation of $[Ru(biq)(phen)(PPh_3)(py)]^{2+}$ following irradiation. Instead CH₃CN substitution must occur from further irradiation of the intermediate, cis– $[Ru(biq)(phen)(CH₃CN)(S)]^{2+}$ where S = coordinating solvent molecule. It is also important to

note that the growth of the ${}^{1}H$ NMR peak corresponding to free CH₃CN at 1.96 ppm for the irradiation of **2a** in CD₃CN shown in Figure 4c does not begin until t ~ 4 min, which is consistent with the dissociation of CH₃CN taking place from the intermediate cis-[Ru(biq)(phen)(CH₃CN)(CD₃CN)]²⁺ and not directly from **2a**.

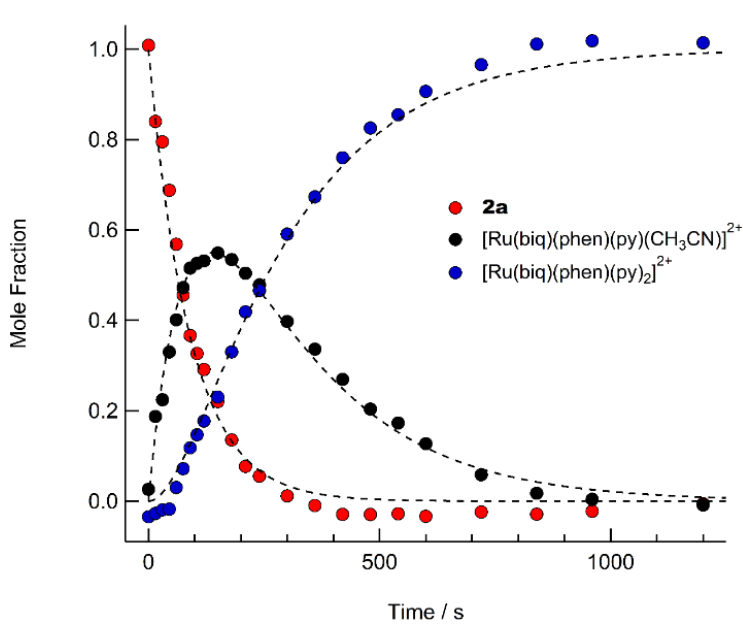


Figure 7. Time dependent concentrations of **2a** (red circles), cis–[Ru(biq)(phen)(py)(CH₃CN)]²⁺ (**I**, black circles), and cis–[Ru(biq)(phen)(py)₂]²⁺ following irradiation ($\lambda_{irr} \ge 395$ nm) in pyridine from t = 0 to t = 1200 s. The dashed lines are least-squares fits to a consecutive reaction model with a system of equations describing the time-dependent concentration of each compound (see text).

In contrast to the results for 2a, the ³¹P{H} NMR of 1a did not change as a function of irradiation time (Figure S14) in CD₃CN, indicating that the PPh₃ ligand is photostable in this complex and does not photodissociate. Together, these results demonstrate the photoinduced ligand exchange of PPh₃ from 2a upon irradiation with $\lambda_{irr} \ge 395$ nm, while 1a undergoes only CH₃CN ligand substitution. Steric strain around the Ru(II) center due to the bulky biq ligand is known to influence the exchange of ligands from Ru(II) complexes following irradiation and likely plays a role in the photoinduced PPh₃ exchange in 2a. ^{41,65,66} The observed trends highlight a need

to further investigate the geometry around the ruthenium center in phosphine complexes to identify the origin of the unusual dissociation of PPh₃ in **2a**.

Structural Comparisons

The generally accepted model for photoinduced ligand exchange in Ru(II) polypyridyl complexes is thermal population of a 3 LF (ligand field) state from a lower energy 3 MLCT (metal-to-ligand charge transfer) state, which places electron density on Ru-L orbital(s) with σ^{*} antibonding character, leading to ligand dissociation. Distortion in the pseudo-octahedral geometry around ruthenium metal lowers the energy of the e_{g} -type σ^{*} set, and consequently of the dissociative 3 LF state, leading to a decrease in the activation energy required to thermally populate it from the lowest energy 3 MLCT state and increasing the efficiency of ligand exchange. The introduction of steric bulk via ligands containing methyl, phenyl, or quinoline moieties has been shown to sufficiently distort the octahedral geometry, resulting in an increase the quantum yield of ligand exchange. ${}^{71-74}$

In order to better understand if steric effects account for the differences in the photoreactivity of **1a** and **2a**, their solid-state single-crystal x-ray structures were determined and are shown in Figure 8, along with relevant bond lengths and angles listed in Table 2 with additional x-ray data available in Tables S3 and S4. The Ru-N bond lengths from the ruthenium center to the bidentate ligand *trans* to the PPh₃ ligand are 0.05 Å longer on average in **2a** (biq) as compared to **1a** (phen), respectively, indicating greater steric strain in the former. The greater steric hindrance in **2a** relative to **1a** is further supported by the Ru1-P1 bond length, which is 0.024 Å longer in **2a**, consistent with a weaker Ru-P bonding interaction in the biquinoline complex. The crystal structure of **2b** (Figure 8), obtained by irradiating a solution of **2a** in CH₃CN with visible light overnight, possesses Ru-N3 and Ru-N4 bond lengths that are 0.075 and 0.028 Å shorter than in **2a**, respectively, where N3 and N4 are the nitrogen atoms in biquinoline ligand. Such a decrease in Ru-N bond lengths demonstrates that the photodissociation of PPh₃ relieves steric strain.

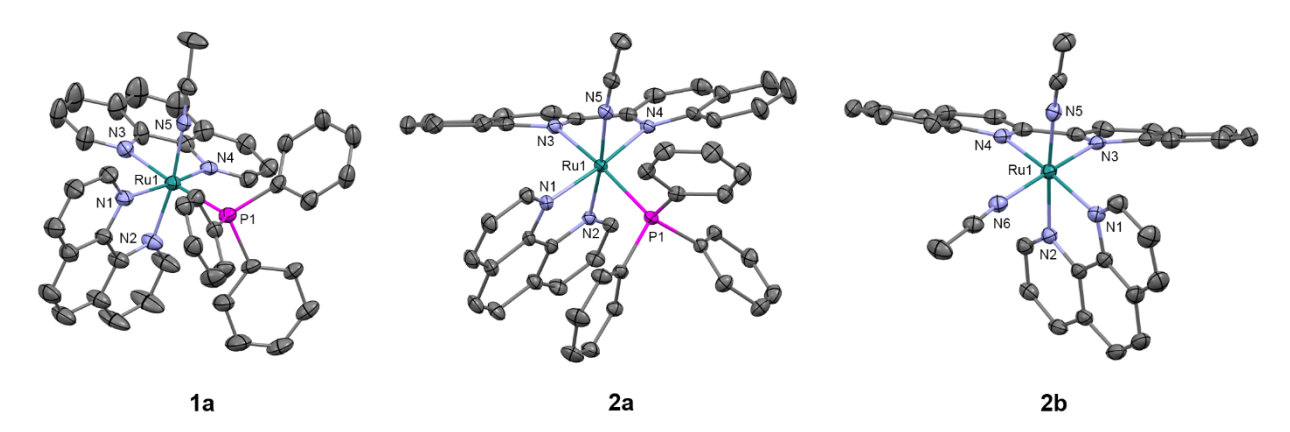


Figure 8. ORTEP plots of **1a**, **2a**, and **2b** (thermal ellipsoids have been drawn at 50% probability and hydrogen atoms, PF₆⁻ molecules, and co-crystallized solvent molecules have been omitted for clarity); Ru: cyan, N: light purple, C: grey, and P: magenta.

Evidence for distortion of the bidentate ligand *trans* to PPh₃ is apparent in the torsion angle, the angle between the two N-C-C planes formed by N3 of the bidentate ligand and the two carbon atoms bridging it to N4, expected to be 0° in an ideal octahedral geometry. In the case of **1a**, the N3-C-C-N4 torsion angle in the phenanthroline ligand is 2(1)°. In contrast, a torsion angle of 10.5(2)° is measured in the biquinoline ligand in **2a**. Further, geometric planes defined by N1-Ru1-N2 and N3-Ru1-N4 would be at 90° angles in an ideal octahedral geometry and deviations from this angle reveal additional steric distortion around the metal center.⁴ The angle between these two planes in **1a** was determined to be 88.69°, which is reduced to 81.37° in **2a**. Importantly, in **2b** this angle is 86.93° and the N3-C-C-N4 torsion angle in the biquinoline ligand is 3.1(3)°, showing the substitution of PPh₃ for CH₃CN allows the complex to adopt a geometry closer to the ideal octahedral. It should be noted that the Ru-N5 bond to the CH₃CN ligand, which dissociates in both complexes, does not significantly differ in length (0.006 Å) in **1a** and **2a**.

The bond angles provided in Table 2 demonstrate additional differences in the steric distortion in **1a**, **2a**, and **2b**. For example, the N1-Ru1-N3 and N2-Ru1-N3 angles show the extent of distortion in the phenanthroline ligand in each complex. Substitution of biq for phen in **2a** pushes N1 towards the phosphine ligand while N2 moves away from P1 to accommodate the large

PPh₃ unit, such that the N2-Ru1-N3 angle is nearly 10° greater in **1a** than **2a**. These same angles in **2b** demonstrate that the dissociation of PPh₃ relieves the steric strain between the polypyridyl bidentate ligands by allowing the phenanthroline ligand to move away from biq.

Table 2. Selected Crystallographic Bond Lengths and Angles for 1a, 2a, and 2b.

Bond lengths (Å)	1a	2a	2b
Ru1-N3	2.106(9)	2.148(1)	2.073(2)
Ru1-N4	2.06(1)	2.112(2)	2.084(2)
Ru1-N5	2.030(2)	2.036(2)	2.046(2)
Ru1-P1/N6	2.343(1)	2.3669(5)	2.034(2)
Torsion angle (°)			
N1-C-C-N2	1.1(4)	2.1(2)	0.6(3)
N3-C-C-N4	2(1)	10.5(2)	3.1(3)
Bond angle (°)			
N1-Ru1-N3	87.7(2)	94.09(9)	100.22(7)
N1-Ru1-P1/N6	93.68(8)	85.26(7)	82.24(7)
N2-Ru1-N3	91.2(2)	81.95(9)	87.52(6)
N3-Ru1-N5	82.1(2)	93.13(9)	93.52(7)
N4-Ru1-P1/N6	98.8(4)	103.63(7)	99.31(7)

The angles N1-Ru1-P1 and N4-Ru1-P1 show the bulkier biquinoline ligand pushes the phosphine away from biq and toward phen in 2a, to a significantly greater extent than in the analogous phen in 1a. Similar to the bond angles, the CH₃CN ligand does not display great distortion. The only notable angle change is that for N3-Ru1-N5, which is 11° smaller in 1a than in 2a, indicating that PPh₃ pushes the acetonitrile ligand towards the *trans* bidentate ligand in 1a but the presence of the larger biq ligand prevents this displacement in 2a. In summary, the x-ray

crystal structures show that there are significantly greater deviations from octahedral geometry in **2a** as compared to **1a** and **2b**.

Calculations

Density functional theory (DFT) calculations were performed to determine if the bonding and electronic structure in the complexes could further explain the differences in the photoreactivity of **1a** and **2a**. Geometry optimizations in the singlet ground state (¹GS) of **1a**, **2a**, and **2b** resulted in structures in good agreement with experimental crystallographic data (Table S4). Table S4 shows that the calculated bond lengths, angles, and torsional angles are in good agreement to those obtained experimentally from the crystal structures of each complex. The ¹GS highest occupied molecular orbitals (HOMOs) in **1a** and **2a** exhibit primarily Ru-d orbital character, as is typical for Ru(II) polypyridyl complexes. ^{63,75–77} The lowest unoccupied molecular orbital (LUMO) in each complex is primarily localized on the ligand *trans* to PPh₃, 1,10-phenanthroline in **1a** and 2,2'-biquinoline in **2a**; the latter agrees with the findings from electrochemistry (Figures S15 and S16 and Table S5).

Geometry optimizations and vibrational frequency calculations were also performed in the triplet excited states (³ES) of **1a** and **2a**. In the ³ES, longer Ru–NCCH₃ and Ru–P bond distances are calculated in both complexes as compared to the corresponding ¹GS (Table 3). The calculated Ru–P bonds in the ³ES are similar, 2.475 Å in **1a** and 2.473 Å in **2a**, increasing from 2.411 Å and 2.441 Å in the ¹GS, respectively. However, the Ru–NCCH₃ bond is 0.04 Å longer in the ³ES of **1a**, 2.055 Å, as compared to that in **2a**, 2.015 Å, which may indicate that the Ru-nitrile bond is weaker in the excited state of **1a** relative to that in **2a**.

The differences in the bonds of **1a** and **2a** in the ³ES were further investigated by calculating the Mayer bond orders (MBOs) of the bonds involving ruthenium (Table 3). MBOs are an extension of Wiberg bond orders and can provide insight into the relative strengths of bonds in transition metal complexes. In the ³ES of **1a**, the MBO of the Ru-NCCH₃ bond (Ru1-N5) exhibits a 26.6% decrease as compared to the ¹GS and the Ru-N(phen) bond *trans* to CH₃CN

(Ru1-N3) displays a dramatic 74.0% increase. These results indicate that the reduced phenanthroline ligand in the excited state exerts a *trans*-type influence on the CH₃CN ligand and weakens the Ru1-N3 bond, likely contributing to its dissociation in the excited state as has been observed in other Ru(II) complexes.^{33,78,79} In contrast, the MBO of the bond to CH₃CN only decreases by 11.8% in the triplet state of **2a** and the order of the Ru-N bond *trans* to CH₃CN does not change in the triplet state of **2a**. In addition, the Ru–NCCH₃ bond itself is significantly stronger in the ³ES of **2a** as compared to **1a**, 0.576 and 0.441, respectively.

Table 3. Selected Mayer Bond Orders, MBOs, in the ¹GS and Lowest ³ES of **1a** and **2a**.

	MBOs			Bond Lengths / Å				
	18	a	2	a	1	la	2	2a
Bond	¹ GS	³ ES	¹ GS	³ ES	¹GS	³ ES	¹GS	³ ES
Ru1-N3 ^a	0.370	0.656	0.223	0.223	2.080	2.022	2.096	2.095
Ru1-N5 ^b	0.601	0.441	0.653	0.576	2.008	2.055	2.000	2.015
Ru1-N1 ^c	0.260	0.408	0.281	0.368	2.136	2.103	2.170	2.146
Ru1-P1	0.760	0.719	0.701	0.659	2.411	2.475	2.441	2.473

^aBond to N atom of bidentate ligand *trans* to CH₃CN. ^bBond to N atom of CH₃CN. ^cBond to N atom of bidentate ligand *trans* to PPh₃.

Both **1a** and **2a** displayed a ~6% increase in the MBO of the Ru-PPh₃ bond, Ru1–P1 in Table 3, in the ³ES, although the the bond is weaker in the excited state of **2a**, MBO = 0.659, than in **1a**, MOB = 0.719. The order of the bond *trans* to the phosphine ligand, Ru1-N1, is calculated to increase by 31.0% in **2a** and 56.9% in **1a**, indicating a *trans*-type influence in both complexes. However, the phenomenon is significantly stronger in **1a** for the bond positioned *trans* to the CH₃CN ligand, Ru1-N3, which may explain why the CH₃CN ligand preferentially photodissociates in this complex.

Mulliken spin density (MSD) calculations were also performed on the lowest energy ³ES of 1a and 2a. These calculations determine the unpaired electron density on each atom in the ³ES and can provide information on the nature of the excited state. In complexes with ³LF as the lowest energy triplet excited state, the spin density on the Ru(II) metal center would theoretically equal two. If the lowest energy ³ES is MLCT in nature, the spin density on ruthenium is expected to be one, and any deviation from these whole numbers indicates metal/ligand mixing. The MSD on ruthenium and the summed density on each ligand in the lowest energy ³ES of **1a** and **2a** is shown in Figure 9. The calculated spin densities on Ru(II) indicate the lowest energy triplet excited state is MLCT in nature with notable ligand character in 1a and significant mixing from a ligandcentered state in 2a. The summed spin density on the phenanthroline ligand trans to PPh₃ in 1a is 0.447, lower than the 0.763 sum on the phen ligand trans to CH₃CN, further indicating stronger trans-type influence on the nitrile ligand in the excited state. In the ³MLCT of 2a the sum of the spin density on the phen ligand, which is trans to CH₃CN, is 0.074 and a sum of 1.433 is calculated on the biquinoline ligand, indicating a significant trans-type influence on the PPh₃ ligand. Taken together with the calculated bond lengths and MBOs in the ³MLCT state, it can be concluded that while 1a exhibits a trans-type influence on both monodentate ligands, it is stronger in the case of the CH₃CN ligand which can explain the preferential dissociation of CH₃CN upon irradiation. In the ³MLCT state of **2a** there is no evidence of *trans*-type influence on the nitrile ligand, but a significant degree of trans-type influence is calculated for the phosphine ligand. These results, in conjunction with the steric strain evident from the crystal structure, can explain the unexpected photodissociation of the PPh₃ ligand in 2a.

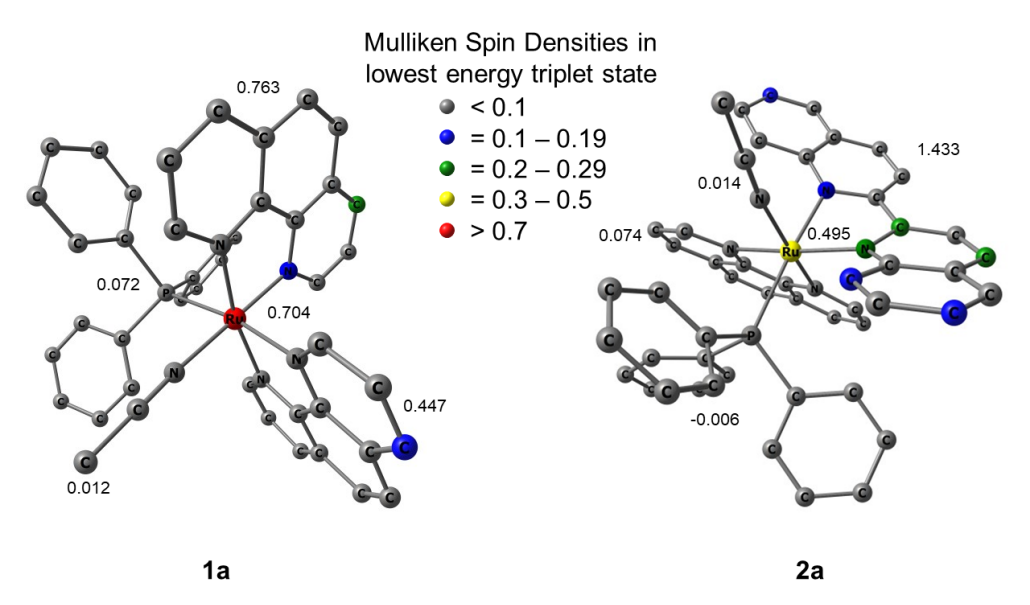


Figure 9. Mulliken spin densities (MSDs) on ruthenium and the summed densities on each ligand in the calculated lowest energy triplet excited states of 1a and 2a.

Cell Viability

The effect of photochemical reactivity on the biological behavior of **1a** and **2a** was investigated on the MDA-MB-231 triple-negative breast cancer cell line in the dark and upon irradiation and the results were compared to those of related complexes previously reported. ^{18,80,81} The half effective concentration, EC₅₀, was determined, which is defined as the concentration of the compound when the viability of the experimental cells is 50% compared to those in the absence of active compound. Complexes **1a** and **2a** were incubated MDA-MB-231 cells for 1 hr and were then either left in the dark or irradiated with blue light for 20 min (λ_{irr} = 460–470 nm, 56 J/cm²). Cellular viability was assessed using the MTT assay after 72 hrs, where the viability upon treatment with only the vehicle control, 1% DMSO in DMEM (Dulbecco's Modified Eagle Medium) was considered as 100%, and the results are listed in Table 3. Both **1a** and **2a** are non-toxic against MDA-MB-231 cells in the dark with EC₅₀^D values of 26.6 ± 1.5 μ M and >30 μ M, respectively; the latter is above the maximum concentration allowed by the solubility in growth media (30 μ M). However, irradiation with blue light significantly increases the toxicities of both

complexes, resulting in EC₅₀^L = $4.6 \pm 0.6 \,\mu\text{M}$ for $1\mathbf{a}$ and EC₅₀^L = $7.1 \pm 0.2 \,\mu\text{M}$ for $2\mathbf{a}$ (Figures S17 and S18). These values of the Phototherapeutic Index, PI, defined as EC₅₀^D/EC₅₀^L, were calculated to be 5.8 and >4.2 for $1\mathbf{a}$ and $2\mathbf{a}$, respectively (Table 4). While complex $1\mathbf{a}$ exchanges CH₃CN for a solvent water molecule, $2\mathbf{a}$ releases PPh₃ upon irradiation. The finding that PPh₃ by itself is not toxic against MDA-MB-231 cells both in the dark and when irradiated with blue light ($t_{irr} = 20 \, \text{min}$, $\lambda_{irr} = 460-470 \, \text{nm}$, $56 \, \text{J/cm}^2$) in the concentrations used for complexes $1\mathbf{a}$ and $2\mathbf{a}$ (Figure S19) lead to the conclusion that the corresponding aqua complexes are the major cause of toxicity upon irradiation.

Table 4. EC₅₀ Values Upon Irradiation and in the Dark and Photochemotherapeutic Index, PI, for **1a**, **2a**, and Related Compounds in MDA-MB-231 Cancer Cells.

Complex	$\mathrm{EC}_{50}^{\mathrm{D}}$ / $\mu\mathrm{M}^{a}$	EC_{50}^{L} / μ M a	PI ^b
1a	26.6 ± 1.5	4.6 ± 0.6	5.8
2a	>30	7.1 ± 0.2	>4.2
$[Ru(bpy)_2(PPh_3)(CH_3CN)]^{2+c}$	>30	7.0 ± 1.4	>4.3
cis-[Ru(bpy) ₂ (CH ₃ CN) ₂] ^{2+ d}	244 ± 23	223 ± 94	1.1 ± 0.4

^aData are an average of three independent experiments. ^bPI = EC_{50}^D/EC_{50}^L . ^cFrom ref. 82; bpy = 2,2'-bipyridine. ^dFrom ref. 83; IC_{50} values against HeLa cells; bpy = 2,2'-bipyridine.

Comparison of the cell toxicity data of *cis*–[Ru(bpy)₂(PPh₃)(CH₃CN)]²⁺ and *cis*–[Ru(bpy)₂(CH₃CN)₂]²⁺ in Table 3 indicates that the substitution of a CH₃CN ligand for PPh₃ increases the PI value of the ruthenium complex. Complexes **1a** and **2a** exhibit PI values similar to or exceeding that of *cis*–[Ru(bpy)₂(PPh₃)(CH₃CN)]²⁺. These results indicate that the phosphine ligand may positively influence the activity against cancer cells of these ruthenium complexes, a conclusion supported by previous examples of phosphines improving cellular uptake and localizing complexes to the mitochondria, increasing selectivity for cancerous cells over healthy cells,²² and increasing cytotoxic activity against breast and colon cancer cells of phosphine containing *cis*-configured Pt(II) complexes over that of cisplatin.^{21,84–86}

Conclusion

Two new triphenylphosphine-containing complexes, 1a and 2a, were synthesized and their ground state spectroscopic and electrochemical properties were characterized, along with their photoinduced ligand exchange and cytotoxicity against a triple-negative breast cancer cell line. Changes in the electronic absorption and NMR spectra of complex 1a revealed the substitution of a CH₃CN ligand for a solvent molecule following visible light irradiation and a substitutionally inert PPh₃. In contrast, the photolysis of complex 2a results in the initial exchange of the PPh₃ ligand generating a solvated intermediate, and the latter goes on to absorb a second photon which then undergoes CH₃CN substitution. A comparison of the single crystal x-ray structures reveals that 2a exhibits greater steric distortion around the metal center than 1a, which is subsequently relieved upon the photoinduced exchange of PPh₃ for a less sterically-demanding solvent molecule. To our knowledge, this represents the first report of the photodissociation of a phosphine ligand from a Ru(II) polypyridyl complex. In addition, the ability of phosphine ligands to enhance cellular uptake was shown to enhance the photocytoxicity of 1a and 2a against a triple-negative breast cancer cell line relative to related complexes without PPh₃ in their coordination sphere. This work shows that a coordinated PPh₃ ligand can serve as a new architecture for potential therapeutics for use in PCT.

Associated Content

Supporting information. The following files are available free of charge. ¹H and ³¹P{H} NMR spectra, electrochemical and X-ray crystallographic data, and DFT information (PDF)

Corresponding Authors. *E-mail: turro.1@osu.edu (C. Turro), jkodanko@wayne.edu (J. J. Kodanko)

Notes The authors declare no competing financial interest.

Acknowledgments. The authors thank the support from the National Science Foundation (CHE-2102508), as well as Dr. J. C. Gallucci for assistance with the collection of the crystal structure data of **2a**.

References

(1) N. A. Smith, and P. J. Sadler, *Philos. Trans. R. Soc. A*, 2013, **371**, 20120519.

- (2) (a) S. B. Vittardi, R. T. Magar, D. J. Breen and J. J. Rack, *J. Am. Chem. Soc.*, 2021, 143, 526-537. (b) A W. King, L. Wang and J. J. Rack, *Acc. Chem. Res.*, 2015, 48, 1115-1122. (c) B. A. McClure, N. V. Mockus, D. P. Butcher, Jr., D. A. Lutterman, C. Turro, J. L. Petersen and J. J. Rack, *Inorg. Chem.*, 2009, 48, 8084-8091.
- (3) (a) J. Karges, S. Kuang, F. Maschietto, O. Blacque, I. Ciofini, H. Chao and G. Gasser, *Nat. Commun.*, 2020, **11**, 1–13. (b) M. Jakubaszek, B. Goud, S. Ferrari, and G. Gasser, *Chem. Commun.*, 2018, **54**, 13040-13059. (c) C. Mari, V. Pierroz, S. Ferrari, and G. Gasser, *Chem. Sci.*, 2015, **6**, 2660-2686.
- (4) (a) J. K. White, R. H. Schmehl and C. Turro, *Inorg. Chim. Acta*, 2017, 454, 7-20. (b) J. D. Knoll, B. A. Albani and C. Turro, *Acc. Chem. Res.*, 2015, 48, 2280–2287. (c) J. D. Knoll and C. Turro, *Coord. Chem. Rev.*, 2015, 282-283, 110-126. (d) Y. Sun, M. El Ojaimi, R. Hammit, R. P. Thummel and C. Turro, *J. Phys. Chem. B*, 2010, 114, 14664-14670.
- S. Monro, K. L. Colon, H. Yin, J. Roque, P. Konda, S. Gujar, R. P. Thummel, L. Lilge, C. G. Cameron and S. A. McFarland, *Chem. Rev.*, 2019, 119, 797–828.
- (6) L. Hammarström, Acc. Chem. Res., 2015, **48**, 840–850.
- (7) M. R. Gill and J. A. Thomas, *Chem. Soc. Rev.*, 2012, **41**, 3179-3192.
- (8) L. Marcelis, J. Ghesquiere, K. Garnir, A. Kirsch-De Mesmaeker and C. Moucheron, *Coord. Chem. Rev.*, 2012, **256**, 1569-1582.
- (9) R. Oun, Y. E. Moussa and N. J. Wheate, *Dalton Trans.*, 2018, 47, 6645–6653.
- (10) R. Liu, L. Zhang, J. Zhao, Z. Luo, Y. Huang and S. Zhao, Adv. Ther., 2018, 1, 1800041.
- (11) J. Dang, H. He, D. Chen and L. Yin, L. Biomater. Sci., 2017, 5, 1500–1511.
- (12) Y. Mir, J. E. van Lier, B. Paquette and D. Houde, *Photochem. Photobiol.*, 2008, **84**, 1182–1186.
- (13) D. Havrylyuk, D. K. Heidary, Y. Sun, S. Parkin and E. C. Glazer, *ACS Omega*, 2020, **5**, 18894-18906.
- (14) H. Shi, C. Imberti and P. J. Sadler, *Inorg. Chem. Front.*, 2019, **6**, 1623–1638.
- (15) V. H. S. van Rixel, V. Ramu, A. B. Auyeung, N. Beztsinna, D. Y. Leger, L. N. Lameijer, S. T. Hilt, S. E. Le Devedec, T. Yildiz, T. Betancourt, M. B. Gildner, T. W. Hudnall, V. Sol, B. Liagre, A. Kornienko and S. Bonnet, *J. Am. Chem. Soc.*, 2019, 141, 18444–18454.
- (16) M. K. Herroon, R. Sharma, E. Rajagurubandara, C. Turro, J. J. Kodanko and I. Podgorski, *Biol. Chem.*, 2016, **397**, 571–582.

- (17) M. Huisman, J. K. White, V. G. Lewalski, I. Podgorski, C. Turro and J. J. Kodanko, *Chem. Commun.*, 2016, **52**, 12590–12593.
- (18) K. Arora, M. Herroon, M. H. Al-Afyouni, N. P. Toupin, T. N. Rohrabaugh, L. M. Loftus, I. Podgorski, C. Turro and J. J. Kodanko, *J. Am. Chem. Soc.*, 2018, **140**, 14367–14380.
- (19) T. N. Rohrabaugh, A. M. Rohrabaugh, J. J. Kodanko, J. K. White and C. Turro, *Chem. Commun.*, 2018, **54**, 5193–5196.
- (20) A. Li, R. Yadav, J. K. White, M. K. Herroon, B. P. Callahan, I. Podgorski, C. Turro, E. E. Scott and J. J. Kodanko, *Chem. Commun.*, 2017, **53**, 3673–3676.
- (21) (a) A. A. Khan, K. S. Allemailen, A. Almatroudi, S. A. Almatroodi, M. A. Alsahli and A. H. Rahmani, J. Drug Deliv. Sci. Tech., 2021, 61, 102315. (b) B. Rousselle, F. Bouyer, J. Bayardon, M. Laly, F. Ghiringhelli, Y. Rousselin, E. Bodio and R. Malacea-Kabbara, Dalton Trans., 2021, 50, 4880-4889. (c) M. Ali, L. Dondaine, A. Adolle, C. Sampaio, F. Chotard, P. Richard, F. Denat, A. Bettaieb, P. Le Gendre, V. Laurens, C. Goze, C. Paul and E. Bodio, J. Med. Chem., 2015, 58, 4521-4528.
- (22) R. S. Correa, L. M. Bomfim, K. M. Oliveira, D. R. M. Moreira, M. B. P. Soares, J. Ellena, D. P. Bezerra and A. A. Batista, *J. Biol Inorg. Chem.*, 2019, **198**, 110751.
- (23) Y. R. Pérez and R. Etchenique, *Photochem. Photobiol. Sci.*, 2019, 18, 208–212.
- (24) S. M. Veronica, M. Alvarez, O. Filevich, R. Etchenique and A. del Campo, *Langmuir*, 2012, **28**, 1217–1221.
- (25) L. Zayat, M. G. Noval, J. Campi, C. I. Calero, D. J. Calvo and R. Etchenique, *Chembiochem*, 2007, **8**, 2035–2038.
- (26) S. K. Lee, M. Kondo, G. Nakamura, M. Okamura and S. Masaoka, *Chem. Commun.*, 2018, **54**, 6915–6918.
- (27) I. M. Dixon, E. Lebon, G. Loustau, P. Sutra, L. Vendier and A. Juris, *Dalton. Trans.*, 2008, 5627–5635.
- (28) E. Lebon, I. M. Dixon, L. Vendier, A. Igau and P. Sutra, *Inorg. Chim. Acta*, 2007, **360**, 1235–1239.
- (29) I. M. Dixon, E. Lebon, P. Sutra and A. Igau, Chem. Soc. Rev., 2009, 38, 1621–1634.
- (30) D. V. Pinnick and B. Durham, *Inorg. Chem.*, 1984, **23**, 1440–1445.
- (31) L. Zayat, O. Filevich, L. Baraldo and R. Etchenique, *Philos. Trans. R. Soc. A*, 2013, **371**, 20120330.
- (32) J. D. Knoll, B. A. Albani and C. Turro, Chem. Commun., 2015, 51, 8777–8780.
- (33) L. M. Loftus, A. Li, K. L. Fillman, P. D. Martin, J. J. Kodanko and C. Turro, *J. Am. Chem. Soc.*, 2017, **139**, 18295–18306.

- (34) T. N. Rohrabaugh, Jr., K. A. Collins, C. Xue, J. K. White, J. J. Kodanko and C. Turro, *Dalton Trans.*, 2018, **47**, 11851–11858.
- (35) W.-S. Huang, S. Liu, D. Zou, M. Thomas, Y. Wang, T. Zhou, J. Romero, A. Kohlmann, F. Li, J. Qi, L. Cai, T. A. Dwight, Y. Xu, R. Xu, R. Dodd, A. Toms, L. Parillon, X. Lu, R. Anjum, S. Zhang, F. Wang, J. Keats, S. D. Wardwell, Y. Ning, Q. Xu, L. E. Moran, Q. K. Mohemmad, H. G. Jang, T. Clackson, N. I. Narasimhan, V. M. Rivera, X. Zhu, D. Dalgarno and W. C. Shakespeare, *J. Med. Chem.*, 2016, 59, 4938-4964.
- (36) R. Wang, Y. Chen, X. Zhao, S. Yu, B. Yang, T. Wu, J. Guo, C. Hao, D. Zhao and M. Cheng, *Eur. J. Med. Chem.*, 2019, **183**, 111716.
- (37) J. Tu, L. T. Song, H. L. Zhai, J. Wang and X. Y. Zhang, *Int. J. Biol. Macromol.*, 2018, **118**, 1149-1156.
- (38) S. Bischoff and M. Kant, Catal. Today, 2001, 66, 183–189.
- (39) A. Riisager, K. M. Eriksen, P. Wasserscheid and R. Fehrmann, *Catal. Let.*, 2003, **90**, 149–153.
- (40) B. A. Harper, D. A. Knight, C. George, S. L. Brandow, W. J. Dressick and C. S. Dalcey, *Inorg. Chem.*, 2003, **42**, 516–524.
- (41) B. A. Albani, C. B. Durr and C. Turro, J. Phys. Chem. A, 2013, 117, 13885–13892.
- (42) Z. Assefa and D. M. Stanbury, J. Am. Chem. Soc., 1997, 119, 521–530.
- (43) M. A. Bennett and A. K. Smith, J. C. S. Dalton, 1974, 233–241.
- (44) A. Alberti, P. Astolfi, P. Carloni, L. Greci, C. Rizzoli and P. Stipa, *New J. Chem.*, 2015, **39**, 8964–8970
- (45) V. V. Pavlishchuk and A. W. Addison, *Inorg. Chim. Acta*, 2000, **298**, 97–102.
- (46) M. J. Frisch, G. W. Trucks, H. B. Schlegel, G. E. Scuseria, M. A. Robb, J. R. Cheeseman, G. Scalmani, V. Barone, G. A. Petersson, H. Nakatsuji, X. Li, M. Caricato, A. Marenich, J. Bloino, B. G. Janesko, R. Gomperts, B. Mennucci, H. P. Hratchian, J. V. Ortiz, A. F. Izmaylov, J. L. Sonnenberg, D. Williams-Young, F. Ding, F. Lipparini, F. Egidi, J. Goings, B. Peng, A. Petrone, T. Henderson, D. Ranasinghe, V. G. Zakrzewski, J. Gao, N. Rega, G. Zheng, W. Liang, M. Hada, M. Ehara, K. Toyota, R. Fukuda, J. Hasegawa, M. Ishida, T. Nakajima, Y. Honda, O. Kitao, H. Nakai, T. Vreven, K. Throssell, J. A. Montgomery, Jr., J. E. Peralta, F. Ogliaro, M. Bearpark, J. J. Heyd, E. Brothers, K. N. Kudin, V. N. Staroverov, T. Keith, R. Kobayahsi, J. Normand, K. Raghavachari, A. Rendell, J. C. Burant, S. S. Iyengar, J. Tomasi, M. Cossi, J. M. Millam, M. Klene, C. Adamo, R. Cammi, J. W. Ochterski, R. L. Martin, K. Morokuma, O. Farkas, J. B. Foresman and D. J. Fox, Gaussian 09, revision E.01. Gaussian, Inc.: Wallingford, CT, 2016.
- (47) D. Andrae, U. Häußermann, M. Dolg, H. Stoll and H. Preuß, *Theor. Chim. Acta*, 1990, 77, 123–141.

- (48) A. Schäfer, H. Horn and R. Ahlrichs, J. Chem. Phys., 1992, 97, 2571–2577.
- (49) J. P. Perdew, K. Burke, and M. Ernzerhof, *Phys. Rev. Lett.*, 1996, 77, 1396.
- (50) J. P. Perdew, K. Burke, K. and M. Ernzerhof, *Phys. Rev. Lett.*, 1996, 77, 3865–3868.
- (51) A. D. Becke, *Phys. Rev. A*, 1988, **38**, 3098–3100.
- (52) C. Lee, W. Yang and R. G. Parr, *Phys. Rev. B*, 1988, **37**, 785–789.
- (53) B. Miehlich, A. Savin, H. Stoll and H. Preuss, *Chem. Phys. Lett.*, 1989, **157**, 200–206.
- (54) Chemcraft; Graphical Software for Visualization of Quantum Chemistry Computations. https://www.chemcraftprog.com.
- (55) S. I. Gorelsky and A. B. P. Lever, J. Organomet. Chem., 2001, 635, 187–196.
- (56) S. I. Gorelsky, AOMix: Program for Molecular Orbital Analysis, 2015.
- (57) A. G. Orpen and N. G. Connelly, J. Chem. Soc. Chem. Commun., 1985, 19, 1310–1311.
- (58) D. M. Klassen, Chem. Phys. Lett., 1982, 93, 383–386.
- (59) M. Mitoraj and A. Michalak, *Organometallics*, 2007, **26**, 6576–6580.
- (60) B. A. Albani, B. Peña, K. R. Dunbar and C. Turro, *Photochem. Photobiol. Sci.*, 2014, 13, 272–280.
- (61) P. Bonneson, J. L. Walsh, W. T. Pennington, A. W. Cordes and B. Durham, *Inorg. Chem.*, 1983, **22**, 1761–1765.
- (62) A. Juris, S. Campagna, V. Balzani, G. Gremaud and A. von Zelewsky, *Inorg. Chem.*, 1988, 27, 3652–3655.
- (63) L. M. Loftus, K. F. Al-Afyouni, T. N. Rohrabaugh, Jr., J. C. Gallucci, C. E. Moore, J. J. Rack and C. Turro, *J. Phys. Chem. C*, 2019, **123**, 10291–10299.
- (64) L. M. Loftus, K. F. Al-Afyouni and C. Turro, *Chem. A Eur. J.*, 2018, **24**, 11550–11553.
- (65) E. Wachter, D. K. Heidary, B. S. Howerton, S. Parkin and E. C. Glazer, *Chem. Commun.*, 2012, **48**, 9649–9651.
- (66) E. Baranoff, J.-P. Collin, J. Furusho, Y. Furusho, A.-C. Laemmel, J.-P. Sauvage, *Inorg. Chem.*, 2002, **41**, 1215–1222.
- (67) J. V. Caspar and T. J. Meyer, *Inorg. Chem.*, 1983, 22, 2444-2453
- (68) B. Durham, J. V. Caspar, J. K. Nagle and T. J. Meyer, *J. Am. Chem. Soc.*, 1982, **104**, 4803-4810.
- (69) B. Durham, J. L. Walsh, C. L. Carter and T. J. Meyer, *Inorg. Chem.*, 1980, 19, 860-865.

- (70) G. H. Allen, R. P. White, D. P. Rillema and T. J. Meyer, *J. Am. Chem. Soc.*, 1984, **106**, 2613-2620.
- (71) J. D. Knoll, B. A. Albani, C. B. Durr and C. Turro, *J. Phys. Chem. A*, 2014, **118**, 10603–10610.
- (72) S. Bonnet, J. P. Collin, J. P. Sauvage and E. Schofield, *Inorg. Chem.*, 2004, 43, 8346–8354.
- (73) A.-C. Laemmel, J.-P. Collin and J.-P. Sauvage, Eur. J. Inorg. Chem., 1999, 383–386.
- (74) B. S. Howerton, D. K. Heidary and E. C. Glazer, J. Am. Chem. Soc., 2012, 134, 8324–8327.
- (75) M. H. Al-Afyouni, T. N. Rohrabaugh, K. F. Al-Afyouni and C. Turro, *Chem. Sci.*, 2018, **9**, 6711–6720.
- (76) M. Abrahamsson, M. Jäger, R. J. Kumar, T. Österman, P. Persson, H. C. Becker, O. Johansson and L. Hammarström, *J. Am. Chem. Soc.*, 2008, **130**, 15533–15542.
- (77) J. Romanova, Y. Sadik, M. R. Ranga Prabhath, J. D. Carey and P. D. Jarowski, *J. Phys. Chem. C*, 2017, **121**, 2333–2343.
- (78) E. Galardon, P. Le Maux, L. Toupet and G. Simonneaux, *Organometallics*, 1998, **17**, 565-569.
- (79) A. C. H. Da Silva, J. L. F. Da Silva and D. W. Franco Dalton Trans., 2016, 45, 4907-4915.
- (80) S. D. Ramalho, R. Sharma, J. K. White, N. Aggarwal, A. Chalasani, M. Sameni, K. Moin, P. C. Vieira, C. Turro, J. J. Kodanko and B. F. Sloane, *PLoS One*, 2015, 10, e0142527/1-e0142527/17.
- (81) N. P. Toupin, S. Nadella, S. J. Steinke, C. Turro and J. J. Kodanko, *Inorg. Chem.*, 2020, **59**, 3919-3933.
- (82) A. P. Lanquist, S. Gupta, M. Al-Afyouni, J. J. Kodanko and C. Turro, *Chem. Sci.*, 2021, **12**, 12056-12067
- (83) B. A. Albani, B. Peña, N. A. Leed, N. A. B. G. de Paula, C. Pavani, M. S. Baptista, K. R. Dunbar and C. Turro, *J. Am. Chem. Soc.*, 2014, **136**, 17095-17101.
- (84) H. Scheffler, Y. You and I. Ott, *Polyhedron*, 2010, **29**, 66-69.
- (85) V. Gandin, A. P. Frenandes, M. P. Rigobello, B. Dani, F. Sorrentino, F. Tisato, A. Björnstedt, Bindoli, A. Sturaro, R. Rella and C. Marzano, *Biochem. Pharmacol.*, 2010, **79**, 90-101.
- (86) C. Icsel, V. T. Yilmaz, B. Cevatemre, M. Aygun and E. Ulukaya, *J. Biol. Inorg. Chem.*, 2020, **25**, 75-87.